applied optics

Experimental demonstration of the hybrid opto-electronic correlator for target recognition

Mehjabin S. Monjur,[1,*] Shih Tseng,[1,2] Mohamed F. Fouda,[1] and Selim M. Shahriar[1,3]

[1]Department of Electrical Engineering and Computer Science, Northwestern University, Evanston, Illinois 60208, USA
[2]Digital Optics Technologies, Rolling Meadows, Illinois 60008, USA
[3]Department of Physics and Astronomy, Northwestern University, Evanston, Illinois 60208, USA
*Corresponding author: mehjabin@u.northwestern.edu

Received 31 October 2016; revised 27 February 2017; accepted 27 February 2017; posted 1 March 2017 (Doc. ID 279606); published 24 March 2017

Optical target recognition using correlators is an important technique for fast verification and identification of images. The hybrid opto-electronic correlator (HOC) recently proposed by us bypasses the need for nonlinear materials such as photorefractive polymer films by using detectors instead, and the phase information is yet conserved by the interference of plane waves with the images. In this paper, we demonstrate experimentally the basic working principle of the HOC architecture using currently available technologies. For matched reference and query images, the output signal shows a sharp peak, indicating a match is found. For an unmatched case, a much lower peak value is observed, indicating no match. We also demonstrate the dependence of the output signal on the phases of the interfering plane waves and describe a technique using an interferometer and a servo for optimizing the output signal. As such, the work reported here paves the way for further development of the HOC for practical applications.

OCIS codes: (100.4550) Correlators; (100.5070) Phase retrieval.

https://doi.org/10.1364/AO.56.002754

1. INTRODUCTION

Target identification and tracking are important in many defense and civilian applications. There is an increased need for detecting and matching biological samples at a high speed and in an efficient manner. Optical correlators provide a simple technique for this task. In recent years, we have been investigating the feasibility of realizing an all-optical high-speed automatic target recognition (ATR) system using the inherent parallelism of optical techniques [1–12]. Other groups have also pursued the development of such correlators [13,14]. The simplest forms of such a system are the Vander Lugt correlator [15,16] and the joint-transform correlator [17–20], both of which are based on holography. Optical correlation has also been implemented in color digital holography using a hydrogen Raman shifter as light source [21]. The primary limitation of such holographic correlators is the poor nature of the materials used for recording. To overcome this constraint, we recently proposed a hybrid opto-electronic correlator (HOC) using only photo-detectors, spatial light modulators (SLM), phase stabilization circuits, and VLSI chips [22]. In the HOC, the amplitude and phase information of the query as well as the reference image are recorded with photo-detectors via interference with plane waves. In this paper, we demonstrate experimentally the basic working principle of the HOC architecture using currently available technologies. We show that, for a matched reference and query image, the output signal shows a sharp peak, indicating a match is found. When dissimilar reference and query images are used, a significantly lower peak value is observed, indicating no match. We also demonstrate the dependence of the output signal on the phases of the interfering plane waves and describe a technique for optimizing the output signal by making use of an interferometer and a servo. These results validate the most important aspects of the scheme proposed in Ref. [22], thus paving the way for further development of the HOC for practical applications.

The rest of the paper is organized as follows. Section 2 presents the experimental setup of the HOC architecture and a summary of the working principles of the HOC. The experimental results are presented in Section 3, where we demonstrate the dependence of the output signal on the phases of the interfering plane waves and the ability of the HOC to distinguish between matching and unmatching queries. The paper concludes with a summary and outlook in Section 4.

2. EXPERIMENTAL SETUP AND WORKING PRINCIPLE OF THE SHIFT-INVARIANT HOC

The overall architecture of the proposed HOC is discussed in detail in Ref. [22], and additional steps needed for scale and

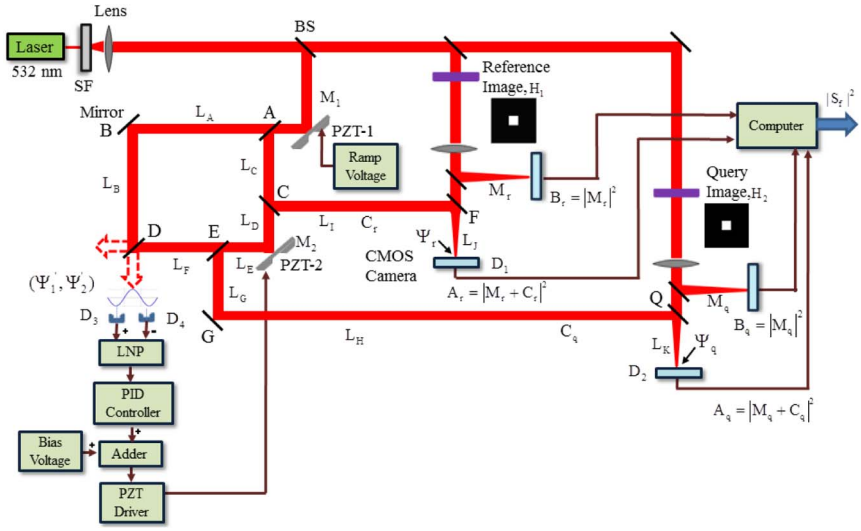

Fig. 1. Simplified architecture of the HOC for demonstrating its basic working principles. See text for details. BS, beam splitter; SF, spatial filter.

rotation invariance are described in Ref. [23]. In describing the architecture of the HOC in Ref. [22], we primarily considered the use of commercially available components, such as cameras, field programmable gate arrays (FPGAs), and SLMs. However, the overall process is severely slowed down during serial communications between these devices. In order for the HOC to achieve its ultimate operating speed, we proposed a novel component called the integrated graphic processing unit (IGPU) [22], which enables the HOC to perform a single correlation operation in a few microseconds. However, the IGPU does not exist currently, and its realization would require a significant development effort. Hence, for now we show the working principle of the HOC using a computer instead of an IGPU.

To demonstrate the basic working principle of the HOC experimentally, we make use of an architecture that is a somewhat simplified version of the one proposed in Ref. [22]. This is illustrated schematically in Fig. 1. A continuous-wave diode-pumped solid-state laser (Verdi V2) with a 532 nm wavelength is used for this experiment. The laser beam has a diameter of 1 mm, which is expanded to 1 in. (2.54 cm) after passing through a spatial filter and a lens. The expanded beam is split into two paths using a 50–50 beam splitter (BS). One path is used for retrieving the images, and the other path is used to create the phase stabilization and scanning circuit (PSSC), which is described in detail in Section 3.A. Instead of using the SLM, as proposed in the original architecture, we have used a portion of the Air Force resolution chart (ARC) to produce the reference and query images. The reference image, H_1, is Fourier transformed (FT) using a lens. The FT image (M_r) is split into two identical ports. In one port, a digital CMOS camera detects the signal M_r. We have used the USB2.0 CMOS camera (DCC1545M), which has 1280 H × 1024 V pixels. The camera is interfaced with a computer via a USB cable. The signal array produced by the camera is denoted as B_r and stored in the computer memory. In the other port, M_r is interfered with a plane wave, C_r, and detected with another CMOS camera, producing the digital signal array A_r. This signal array is also stored in the memory of the computer. These can be expressed as

$$\begin{aligned} A_r &= |M_r e^{j\phi_r} + C_r e^{j\psi_r}|^2 \\ &= |M_r|^2 + |C_r|^2 + |M_r||C_r| e^{j(\phi_r - \psi_r)} \\ &\quad + |M_r||C_r| e^{-j(\phi_r - \psi_r)}, \end{aligned} \tag{1}$$

$$B_r = |M_r|^2. \tag{2}$$

Here $\phi_r(x, y)$ is the phase of the FT image, M_r, and Ψ_r is the phase of the plane wave, C_r, at the detector, D_1. In addition, the intensity profile of the plane wave ($|C_r|^2$) is measured by blocking the image path momentarily using a shutter (not shown). A MATLAB script then uses the stored data to compute the signal, S_r, according to the following equation:

$$\begin{aligned} S_r &= A_r - B_r - |C_r|^2 = M_r C_r^* + M_r^* C_r \\ &= |M_r||C_r| e^{j(\phi_r - \psi_r)} + |M_r||C_r| e^{-j(\phi_r - \psi_r)}. \end{aligned} \tag{3}$$

In a manner similar to what is described above, the query image, H_q, is transferred to an optical beam using another ARC and split into two paths after going through FT with a lens. The resulting image in each path is designated as M_q. In one port, another CMOS camera detects the FT image, with the detected signal being denoted as B_q. In the other port, M_q is interfered with a plane wave, C_q, and detected with another CMOS camera, producing the digital signal array A_q. Using the same MATLAB script mentioned above, we can calculate the signal S_q as

$$\begin{aligned} S_q &= A_q - B_q - |C_q|^2 = M_q C_q^* + M_q^* C_q \\ &= |M_q||C_q| e^{j(\phi_q - \Psi_q)} + |M_q||C_q| e^{-j(\phi_q - \Psi_q)}. \end{aligned} \tag{4}$$

Here, $\phi_q(x, y)$ is the phase of the FT image, M_q, and Ψ_q is the phase of the plan wave C_q at the detector D_2. In the final stage of the HOC, these two signals (S_r and S_q) are multiplied together. The resulting signal array, S, can be expressed as

$$S = S_r \cdot S_q = [\alpha^* M_r M_q + \alpha M_r^* M_q^* + \beta^* M_r M_q^* + \beta M_r^* M_q], \quad \textbf{(5a)}$$

$$S = |C_r||C_q||M_r||M_q|[\cos(\Psi_r + \Psi_q - \phi_M) + \cos(\Psi_r - \Psi_q - \tilde{\phi}_M)], \quad \textbf{(5b)}$$

where $\alpha \equiv |C_r||C_q|e^{j(\psi_r+\psi_q)}$, $\beta \equiv |C_r||C_q|e^{j(\psi_r-\psi_q)}$, $M_r M_q = |M_r||M_q|e^{j\phi_M(x,y)}$, and $M_r M_q^* = |M_r||M_q|e^{j\tilde{\phi}_M(x,y)}$.

According to the original architecture of the HOC, the signal array, S, would be transferred to the optical domain using an SLM. The optical image produced by the SLM would go through FT using a lens and be detected by a focal plane array (FPA). The output of the FPA would provide the main correlation signal. The final signal would thus be expressed as

$$|S_f|^2 = |\alpha^* F(M_r M_q) + \alpha F(M_r^* M_q^*) + \beta^* F(M_r M_q^*) + \beta F(M_r^* M_q)|^2 \quad \textbf{(6a)}$$

$$= 16|C_r|^2|C_q|^2|T|^2 \cos^2\Psi_r \cos^2\Psi_q, \quad \textbf{(6b)}$$

Here, F stands for the Fourier transform, and, in deriving Eq. (6b), we have considered the special case where H_1 and H_2 are symmetrical in both the x and y directions, and we defined $T = F(M_r M_q) = F(M_r^* M_q^*) = F(M_r M_q^*) = F(M_r^* M_q)$. In the experimental result reported here, we calculate the final output signal using Eq. (6a) with MATLAB instead of going to the optical domain again. It is obvious from Eq. (6a) that the final signal is a sum of four terms; the first two terms correspond to the convolution of the reference and the query images, H_1 and H_2, respectively. The last two terms correspond, respectively, to the cross-correlation and anti-cross-correlation of H_1 and H_2. The cross-correlation signal is usually used to find matches between two objects. If a match is found between the reference and the query images, the output signal gives a sharp peak, whereas, for unmatched images, a sharp peak is not observed. The convolution terms can be washed out by implementing the PSSC, which is described in detail in Section 3.A. Since we are limiting our discussion to centered and symmetric images, the cross-correlation and the convolution terms are identical and overlap one another. Hence, it is not necessary to eliminate the convolution terms in this case.

As can be seen from Eq. (6b), the output signal of the HOC depends on the phases of the reference plane waves. Thus, it is important to ensure that the optical path lengths in the experiment are highly stable. In order to achieve the requisite degree of stability, we made use of very rigid optical mounts. Furthermore, the whole experiment was encased in a plexi-glass enclosure to eliminate path length fluctuations due to air currents. Finally, the optical table was floated in order to provide isolation from vibrations.

3. EXPERIMENTAL RESULTS

A. Demonstration of the Phase Stabilization and Control Process

As we have mentioned in Section 2, the output of the laser is split into two paths. One path is used for generating images, and the other path is used for generating the reference beams, C_r and C_q, along with the beams for the PSSC. On the second path, an auxiliary Mach–Zehnder interferometer (MZI) is established in order to control and/or vary the phase difference between the reference beams C_r and C_q. The interference pattern, along with a servo and a PZT (PZT-2), is used to lock the difference of the reference beam phases, Ψ_r and Ψ_q, to a desired value.

From Eq. (5b), it is obvious that the final signal $|S_f|^2$ depends nontrivially on Ψ_r and Ψ_q. In Eq. (5b), the first term corresponds to the convolution, and the second term corresponds to the cross-correlation. Figure 1 shows the architecture for the PSSC, where $(\Psi_r - \Psi_q)$ is kept to a constant value using a simple interferometer along with a feedback loop. Using a PZT (PZT-1) mounted on a mirror before the beam is split for the interferometer and applying a saw-tooth type ramp voltage to it results in a repeated linear scan of $(\Psi_r + \Psi_q)$ over a range of 2π. While scanning is going on, the signal S can be passed through a low-pass filter (LPF) with a bandwidth less than ω_s so that the last term that corresponds to cross-correlation is passed. Such a filter can be easily implemented with an FPGA. The low-pass-filtered version of S goes through FT using a lens and is detected by an FPA, producing only the cross-correlation signals. However, this feature was not used in the experimental data reported here. For the proof of principle experimental demonstration of the PSSC, we only show that the MZI, along with the feedback loop, is capable of securing the phase difference $(\Psi_r - \Psi_q)$ to a desired value, as described in detail below.

To create the MZI, the beam reflected from mirror M_1 is split into two paths using the beam splitter (BS) called A. The first one follows the path $L_A - L_B$, whereas the second one follows the path $L_C - L_D - L_E - L_F$. The two beams are combined using a second BS called D, which creates an interference pattern. At the MZI detector plane (D_3 and D_4), the phase of the beam of the upper path is denoted as Ψ_1', and the phase of the beam in the lower path is denoted as Ψ_2'. The reference beams C_r and C_q start from a common BS (A). The first reference beam C_r follows the path $L_C - L_I - L_J$ to the detector D_1, and the second reference beam C_q follows the path $L_C - L_D - L_E - L_G - L_H - L_K$ to the detector D_2. The phase of C_r at D_1 is denoted as Ψ_r, and that of C_q at D_2 is denoted as Ψ_q. It can be shown that $(\Psi_r - \Psi_q)/k = (\Psi_1' - \Psi_2')/k + \xi$, where k is the wavenumber, and $\xi = (L_C + L_F + L_I + L_J) - (L_A + L_B + L_G + L_H + L_K)$ is the path-length difference. The mirror M_2 (attached to PZT-2) on the path of C_q is used to control the value of $(\Psi_r - \Psi_q)$ while keeping Ψ_r constant. A feedback loop, along with a servo, can adjust the position of PZT-2, which in turn adjusts the value of $(\Psi_1' - \Psi_2')$. This also controls the difference phase $(\Psi_r - \Psi_q)$, assuming that the path-length difference indicated by the parameter ξ is kept constant.

A pair of matched detectors (D_3 and D_4) detects the MZI interference signal. The matched detectors were built using two photodiodes (FDS02). The difference between the voltage outputs of these detectors is generated and amplified by a low-noise pre-amplifier (LNP) of model SR560. The output of the LNP is denoted as the error signal, which is fed to an analog PID controller (SIM960). The output from the PID controller is

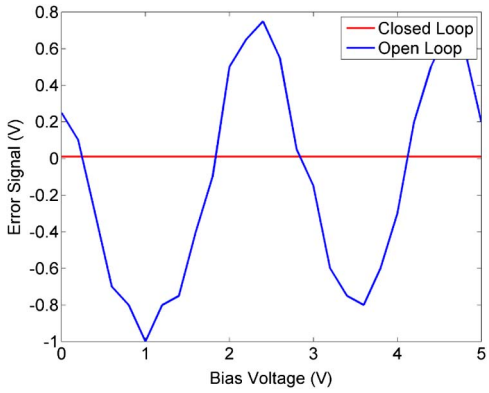

Fig. 2. Experimental demonstration of the feedback loop to stabilize the phases of the plane waves. See text for details.

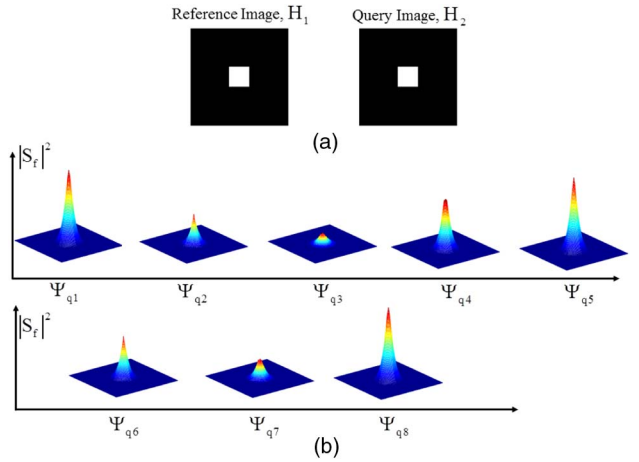

Fig. 3. (a) The reference and the query images. (b) Simulation result of the output signal varying with phase Ψ_q, with the phase Ψ_r remaining constant.

combined with a bias voltage using an adder circuit, and the output of this adder is fed to PZT-2 via a PZT driver. If the error signal is zero, no signal is applied to PZT-2. However, if the interference fringe moves, the error signal and the feedback loop adjust the position of PZT-2 until the interference fringe comes to the position that returns the error signal to zero. The bias voltage can move the relative phase $(\Psi_r - \Psi_q)$ to a different value, and the feedback loop can lock the system to that position. Thus, the feedback loop is used to lock the system at any desired value of $(\Psi_r - \Psi_q)$. In Fig. 2, we illustrate the operation of this servo system while applying a linearly ramping bias voltage (HP Model 6236B Triple Output Power Supply). As can be seen, the error signal varies sinusoidally when the servo is in the open-loop (unlocked) position. However, when the servo is locked (closed-loop operation), the error signal remains at zero, as expected.

While the image detection process is going on, the stability of the phases should be checked after some characteristic time, T_c. This characteristic time is defined as the time during which $(\Psi_r - \Psi_q)$ can drift within a certain allowable range, for example, a few milliradians. After time T_c, we have to adjust the bias voltage again and perform several correlations of two known images with the HOC to get the highest correlation peaks. The characteristic stability time would depend on the stability of the optical mounts and can easily exceed hundreds of seconds in a well-designed system.

B. Phase Dependence of the Output Signal

From Eq. (6), it can be seen that the final signal S_f depends nontrivially on Ψ_r and Ψ_q. Figure 3 shows the simulation result of the output signal when the phase Ψ_q is varied between 0 to 2π while keeping Ψ_r constant. For this particular example, the reference and the query are identical images, as shown in Fig. 3(a). Since the reference and the query images are both positioned at the center, the four terms in Eq. (6a) overlap with one another at the center. As can be seen from Fig. 3(b), the peak value of the signal varies significantly as a function of Ψ_q. We have verified this dependence experimentally, as described below.

We retrieved two identical images from two different ARCs to be used as the reference and the query images. As discussed in Section 2, the terms A_r, B_r, C_r, A_q, B_q, and C_q were captured via a CMOS camera and transferred to the computer via a USB cable. The final output signal $|S_f|^2$ was calculated using a MATLAB script in the local computer. Using the technique described in Section 3.A, we operated the system in the closed-loop mode while applying a variable bias voltage. Thus, the value of Ψ_r was kept constant, and different values of Ψ_q were realized for different bias voltages.

Figure 4(a) shows the experimental results where the amplitude of the output signal, normalized to its peak value, is plotted as a function of the bias voltage. Ideally, Ψ_q, the phase of the plane wave, C_q, is expected to be directly proportional to this bias voltage. Thus, the plot in Fig. 4(a) can, equivalently, be viewed as a display of the signal as a function of Ψ_q. In our current experimental setup, it is not possible to measure the value of Ψ_r. This constraint precludes a quantitative comparison of the experimental result with the prediction of the theoretical model. In Figs. 4(b)–4(f), we have plotted the theoretically expected signal amplitude (normalized to the peak value for $\Psi_r = 0$) as a function of Ψ_q for five different values of Ψ_r:0°, 45°, 90°, 135°, 180°. The range of Ψ_q in each of these plots matches the corresponding range of Ψ_q in Fig. 4(a). As can be seen, the numbers of oscillating cycles in the theoretical plot agree with those in the experimental data. The only distinction among the five theoretical plots is in the peak amplitude. Comparing the experimental data with these plots, we can only surmise that the value of Ψ_r (mod π) is not close to $\pi/2$ but remains fixed during the scan over Ψ_q. This stability of Ψ_r makes the demonstration of the HOC functionality possible. Of course, as discussed in detail in Ref. [22], it is also possible to average over the values of Ψ_r by scanning PZT-1, thereby eliminating the component in the signal contributed by the convolution process and keeping only the part due to the cross-correlation.

In the theoretical plots shown in Fig. 4, we have assumed that the interference processes are ideal, which would correspond to 100% visibility of fringes if, for example, at the detector D_1, the image were a plane wave with an intensity matching that of the reference beam, C_r. The actual

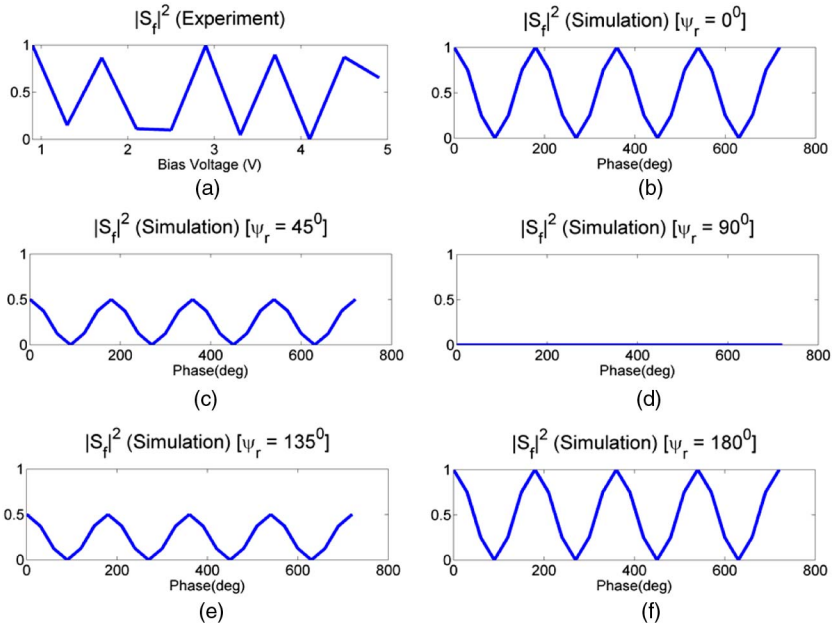

Fig. 4. Comparison of the experimental result (a) and the theoretical model (b)–(f), illustrating how the amplitude of the output signal varies sinusoidally with the applied bias voltage or the phase. See text for details.

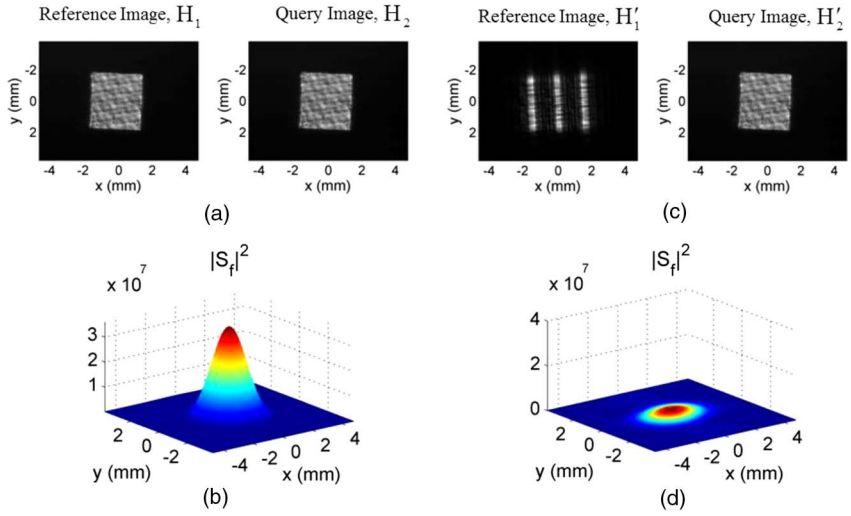

Fig. 5. Experimental results of the HOC for identical images and unmatched images. See text for details.

experimental condition is not close to such ideality. As a result, we observed a small dc bias in the amplitude of the signal as a function of Ψ_q. This dc bias has been subtracted out in generating the plot shown in Fig. 4(a). Finally, it should be noted that there is an unexpected plateau in the data shown in Fig. 4(a). We believe this is due to a localized anomaly in what is otherwise expected to be a linear relationship between and the bias voltage applied to PZT-1.

C. Object Detection Using the HOC

Figure 5 illustrates the experimental results showing the behavior of the HOC for a set of identical reference and query images and for a set of unmatched reference and query images. Figure 5(a) shows the case where the reference image H_1 and the query image H_2 are each a square and placed at the center of the image plane. For such a case, the convolution and cross-correlation terms of Eq. (6) overlap with one another, as discussed earlier. Figure 5(b) shows the experimental result of the output signal, $|S_f|^2$, which has a sharp peak at the center, indicating that a match is found. The amplitude of the signal was maximized by adjusting the value of (i.e., the bias voltage applied to PZT-1). Figure 5(c) shows another case where two different images, H_1' and H_2', are used as the reference image and the query image, respectively. Since they are not matched, we expect to get a lower peak in the output signal compared to the matched case. Figure 5(d) shows the peak value of the

output signal for unmatched images after maximizing via the adjustment of Ψ_q. As can be seen, it is ∼14 times lower than the result for the matched case.

4. CONCLUSION

Our proposed HOC is capable of detecting objects rapidly, while overcoming the material problems of conventional optical correlators by using only photo-detectors, an SLM, and VLSI chips. In this paper, we demonstrate experimentally the basic working principles of the HOC architecture. We show that the HOC is capable of determining whether a match is found or not between a reference image and a query image. We demonstrate that the peak amplitude of the output signal for a matched case is ∼14 times higher than that for an unmatched case. We also show that the output signal varies as a function of the phases of the interfering plane waves and demonstrate a technique for optimizing the output signal using an interferometer and a servo. The work reported here paves the way for further development of the HOC for practical applications.

Funding. Air Force Office of Scientific Research (AFOSR) (FA9550-10-01-0228).

REFERENCES

1. A. Heifetz, G. S. Pati, J. T. Shen, J. K. Lee, M. S. Shahriar, C. Phan, and M. Yamomoto, "Shift-invariant real time edge-enhanced Vander Lugt correlator using video-rate compatible photorefractive polymer," Appl. Opt. **45**, 6148–6153 (2006).
2. A. Heifetz, J. T. Shen, J.-K. Lee, R. Tripathi, and M. S. Shahriar, "Translation-invariant object recognition system using an optical correlator and a super-parallel holographic RAM," Opt. Eng. **45**, 025201 (2006).
3. H. N. Yum, P. R. Hemmer, R. Tripathi, J. T. Shen, and M. S. Shahriar, "Demonstration of a simple technique for determining the *M*/# of a holographic substrate by use of a single exposure," Opt. Lett. **29**, 1784–1786 (2004).
4. M. S. Shahriar, R. Tripathi, M. Huq, and J. T. Shen, "Shared hardware alternating operation of a super-parallel holographic optical correlator and a super-parallel holographic RAM," Opt. Eng. **43**, 1856–1861 (2004).
5. M. S. Shahriar, M. Kleinschmit, R. Tripathi, and J. Shen, "Super-parallel holographic correlator for ultrafast database search," Opt. Lett. **28**, 525–527 (2003).
6. M. S. Shahriar, L. Wong, M. Bock, B. Ham, J. Ludman, and P. Hemmer, "Ultra-high density optical data storage," in *Symposium on Electro-Optics: Present and Future*, H. Haus, ed., Optical Society of America Book Series on Trends in Optics, and Photonics (Optical Society of America, 1998), pp. 97–104.
7. A. Heifetz, J. T. Shen, S. C. Tseng, G. S. Pati, J.-K. Lee, and M. S. Shahriar, "Angular directivity of diffracted wave in Bragg-mismatched readout of volume holographic gratings," Opt. Commun. **280**, 311–316 (2007).
8. D. Sazbon, Z. Zalevsky, E. Rivlina, and D. Mendlovic, "Using Fourier–Mellin-based correlators and their fractional versions in navigational tasks," Pattern Recogn. **35**, 2993–2999 (2002).
9. D. Asselin and H. H. Arsenault, "Rotation and scale invariance with polar and log-polar coordinate transformation," Opt. Commun. **104**, 391–404 (1994).
10. J. Rosen and J. Shamir, "Scale invariant pattern recognition with logarithmic radial harmonic filter," Appl. Opt. **28**, 240–244 (1989).
11. D. Casasent and R. L. Herold, "Novel hybrid optical correlator: theory and optical simulation," Appl. Opt. **14**, 369–377 (1975).
12. D. Casasent, "Hybrid optical/digital image pattern recognition: a review," Proc. SPIE **0528**, 64–82 (1985).
13. J. Khoury, M. C. Golomb, P. Gianino, and C. Woods, "Photorefractive two-beam-coupling nonlinear joint-transform correlator," J. Opt. Soc. Am. B **11**, 2167–2174 (1994).
14. Q. Tang and B. Javidi, "Multiple-object detection with a chirp encoded joint transform correlator," Appl. Opt. **32**, 5079–5088 (1993).
15. S. Jin, Y. Bae, and S. Lee, "Generalized Vander Lugt correlator as an optical pattern classifier and its optimal learning rate," Opt. Commun. **206**, 19–25 (2002).
16. A. V. Lugt, "Signal detection by complex spatial filtering," IEEE Trans. Inf. Theory **10**, 139–145 (1964).
17. B. Javidi and C. Kuo, "Joint transform image correlation using a binary spatial light modulator at the Fourier plane," Appl. Opt. **27**, 663–665 (1988).
18. G. Keryer and J. L. Tocnaye, "A multichannel joint transform correlator," Opt. Commun. **118**, 102–113 (1995).
19. M. S. Alam and M. A. Karim, "Fringe-adjusted joint transform correlation," Appl. Opt. **32**, 4344–4350 (1993).
20. B. Javidi, F. Parchekani, and Q. Tang, "Gray-scale nonlinear joint transform correlator," Opt. Eng. **31**, 888–895 (1992).
21. P. Almoro, W. Garcia, and C. Saloma, "Colored object recognition by digital holography and a hydrogen Raman shifter," Opt. Express **15**, 7176–7181 (2007).
22. M. S. Monjur, S. Tseng, R. Tripathi, J. Donoghue, and M. S. Shahriar, "Hybrid optoelectronic correlator architecture for shift invariant target recognition," J. Opt. Soc. Am. A **31**, 41–47 (2014).
23. M. S. Monjur, S. Tseng, R. Tripathi, and M. S. Shahriar, "Incorporation of polar Mellin transform in a hybrid optoelectronic correlator for scale and rotation invariant target recognition," J. Opt. Soc. Am. A **31**, 1259–1272 (2014).